Correction of B-scan distortion for optimum ultrasonic imaging of back walls with complex geometries

Santi Davì[1], Carmelo Mineo[1], Charles MacLeod[1], Gareth Pierce[1], Anthony Gachagan[1], Scott Paton[2], Gavin Munro[2], Janet O'Brien-O'Reilly[2], Coreen McCubbin[2]

[1] Centre of Ultrasonic Engineering, Dept. of Electronic and Electrical Eng., University of Strathclyde, Glasgow, United Kingdom
santi.davi@strath.ac.uk

[2] Spirit AeroSystems (Europe) Limited, Prestwick, United Kingdom

Abstract – Ultrasound undergoes refraction and reflection at interfaces between media of different acoustic refractive indices. The most common ultrasonic method (pulse-echo) monitors the reflected energy to infer the presence of flaws, whereas the lower amplitude of refracted signals is ignored. When the reflector is oriented normally, with respect to the ultrasonic beam, the received echo signal shows the maximum amplitude. The pulse-echo method also relies on monitoring the amplitude of the back wall echo, to identify or confirm the presence of defects. This works well for parts with constant thickness and with planar back walls. Unfortunately, parts with complex back walls are common to many industrial sectors. For example, in applications such as aerospace structures often require parts with complex shapes. Assessing such parts reliably is not trivial and can cause severe downtimes in the aerospace manufacturing processes or in in-service inspections. This work aims to improve the ultrasonic inspectability of parts with complex back walls, through sending ultrasonic beams from the front wall side. Ultrasonic phased array probes and state-of-the-art instrumentation allow sending ultrasonic energy into a part at wide ranges of focusing depths and steering angles. This allows tracking the back wall profile, thus hitting it normally and maximizing the amplitude of the reflected echo at any point. However, our work has shown that a cross-sectional scan resulting from multiple ultrasonic beams, which are sent at variable incidence angles, can present significant geometrical distortion and can be not of much use for accurate defect visualization and sizing. This paper introduces a generalized algorithm developed to remove geometric distortions and the effect that variable refraction coefficients have on the transmitted and received amplitudes. The algorithm was validated through CIVA simulations for two example parts with complex back walls, considering isotropic materials.

Key words: Ultrasonic imaging; Complex geometries; Data visualization; B-scans.

1. Introduction

1.1 Ultrasonic imaging of complex geometries

Ultrasonic imaging has become the most common technique for non-destructive testing (NDT) of solid structures [1]. Using ultrasound for testing purposes has significant advantages: high penetration for a wide range of materials, capability of estimating the size, orientation, shape and nature of defects and capability of evaluating the structure of alloys of components with different acoustic properties [2]. Moreover, ultrasonic NDT methods are non-hazardous to operations or to nearby personnel and have no effect on equipment and materials in the vicinity. Ultrasonic testing is also easy to deploy through portable equipment or highly automated approaches for large structures.

However, ultrasonic energy is strongly attenuated by air gaps, due to the low acoustic impedance of air. A suitable coupling medium is needed to transfer the ultrasonic waves from the transducer to the material undergoing inspection. Coupling is often achieved by immersion of both the transducer and the specimen in a body of liquid or by actual contact through a thin film of liquid. The ultrasonic vibrations pass through the coupling medium and are reflected by any discontinuities, which may be encountered. The reflected energy is received by the same or by a different transducer and is converted into an electrical signal. Imaging the profile of a complex geometry part, through a rigid linear array transducer, can prove problematic (where direct contact is not always possible). Therefore, this is overcome by coupling through an

intermediate medium such as a Perspex shoe or a fluid, as in the case of immersion testing. However, the computational complexity involved in imaging through a dual media makes real-time inspection difficult, as variations in geometry directly influence the imaging algorithms. Considering the Fermat's principle, an ultrasonic ray starting at a given point arrives to another point following the lowest time of flight path. As a consequence, in presence of a curved interface separating two media with different sound velocities, the lowest time of flight path can diverge from a single straight segment [3]. Since the introduction of advanced ultrasonic data acquisition and imaging techniques, such as full matrix capture (FMC) and the total focusing method (TFM) [4], imaging through a non-planar surface is a time-intensive task [5], where it is necessary to calculate the time of flight from each transmit/receive element combination to a given pixel in the region of interest through the refractive boundary. Extensive investigation has been undertaken in the efficient imaging of such data in post-processing, due to large amount for data storage [6-8] and in real-time inspection [5]. However, the large datasets associated with FMC and the number of calculations required to effectively image ultrasonic data for a complex geometry is still limiting the scanning speed rates [9]. This is a bottleneck in the production of large high-value and safety-critical structures, where robust assessment of structural integrity is an unavoidable requirement.

1.2 Need to increase speed and improve part inspectability

To meet future demand projections (e.g. in the aerospace sector) and overcome the bottlenecks of safety critical NDT inspections, new automated scanning systems have been developed by a variety of research and development teams [10-13]. Producing reliable automated solutions has become an industry priority to drive down inspection times and ensure repeatability. Applications of six-axis robotic arms in the NDT field have been published and there is a growing interest in using such automation solutions [14-18]. In aerospace transportation, the need to reduce operational costs and CO_2 emission into the environment, is leading to aircrafts that are more efficient [19]. Design engineers are focusing on reducing the structural weights by using innovative materials and geometries. Research has enabled the generation of optimum robotic tool-paths to inspect curved parts [20, 21], the introduction of suitable ultrasonic coupling techniques (e.g. purposely developed water-jet nozzles [17] and rolling water chambers [22]) and high data transfer rates. State-of-the-art ultrasonic phased array instrumentation and fast communication sockets have enabled component scanning rates up to 117.6m^2/hour with a robotically manipulated 5MHz 64-element (1mm pitch) phased array transducer, when acquiring frames (B-scans) at 1mm intervals and firing all probe elements at once (thus using an unfocused ultrasonic beam) [23]. The scanning rate of such systems drops to 25m^2/hour, when using traditional beamforming with an 8-element sub-aperture. Indeed, 57 firings are required to sweep the ultrasonic beam through the phased array probe and the maximum robotic manipulation speed is limited to 150mm/s. The figures are worse for phased array FMC; it has typically not yet been used for robotic inspection of large structures, due to the currently achievable low frames per second (FPS). Real-time FMC imaging is currently performed at up to 40 FPS [5], which would limit the scanning rate to around 6.5m^2/hour.

Therefore, although research and technology advancement will speed up FMC and TFM imaging in the future, automated ultrasonic phased array inspection is to date mostly performed through traditional beamforming or the emerging multi-aperture excitation mode [24]. These data acquisition approaches work very well for imaging all part regions that present constant or gently changing thicknesses, as in such scenario a strong back wall reflection is received. Conversely, regions with severe back wall tapering or with complex back walls (e.g. radii) are notoriously challenging to inspect, since the back wall reflects the ultrasonic energy at high angles with respect to the incident beam and the received echo is often not received or strongly attenuated. Previous work has demonstrated the possibility to inspect the radii of structural

stiffening stringers and ribs using concave probes, placing them coaxially to the radii surface, when inspecting from the radii side, or phased array probes defining appropriate delay laws [21, 25-27]. Although this approach maximizes the ultrasonic energy that enters the part, it does not solve the fact that the back wall reflection is often impossible to receive. Moreover, the quality of such an inspection is strongly dependent on the accuracy of the geometric alignment between the probe and the centre of curvature of the radii. Furthermore, the complex geometry side of the part is often not accessible, especially for in-service components, and can present restricted areas where probe placement is difficult.

This paper is focusing on improving the ultrasonic inspectability of parts with complex back walls. Progress in this direction is being achieved by modelling the ultrasonic wave propagation in such parts. Promising results are possible through using state-of-the-art instrumentation that allows exploiting complex focal laws to send ultrasonic energy into a part at wide ranges of focal depths and steering angles. This allows tracking the back wall profile, thus allowing normal angles of incidence and maximizing the amplitude of the reflected echo at any point. This paper presents a new algorithmic approach to improve the visualization of inspection results, relative to regions with complex back walls. Ultrasonic data can be collected and displayed in a number of different formats. Previous work has highlighted the importance of introducing new data visualization and analysis tools capable of mapping complex geometries and enabling easy detection of defects [12, 28-31].

B-scan resulting from multiple A-scans, which originate from ultrasonic beams sent at variable incidence angles, can present significant geometrical distortion and cannot be directly used for accurate defect visualization and sizing. Therefore, this paper introduces a generalized algorithm developed to remove geometric distortions and the effect that variable refraction coefficients have on the transmitted and received amplitudes. This work has focused on isotropic materials as a proof-of-concept phase.

2. Review of current visualization approaches

Strictly speaking, the B-Scan presentation refers to the image produced when the data collected from an ultrasonic inspection is plotted on a cross-sectional view of the component. The original definition, according to BS EN 1330-4:2000, is the "Image of the results of an ultrasonic examination showing a cross-section of the test object perpendicular to the scanning surface and parallel to a reference direction." The cross-section is the plane through which the individual A-scans have been collected. Therefore, the B-scan will generally be the plane that contains the ultrasonic beam axes.

Phased array probes use an array of elements, all individually wired, pulsed and time-shifted on both pulsing and receiving. In traditional beamforming scanning mode, the elements are typically pulsed in groups (known as sub-apertures). With user-friendly systems, a typical set-up calculates the time-delays from operator-input, or uses a pre-defined file calculated for the inspection angle, focal distance and scan pattern [32]. The time delay values are back-calculated using time-of-flight from the focal spot, and the scan assembled from individual 'Focal Laws'. Time delay circuits use high-resolution clocks (nanosecond resolution) to allow pulsing every element and receiving from each element at the required time.

Phased array electronic pulsing and receiving have introduced significant opportunities for a variety of scan patterns. Multiplexing along an array generates electronic scans (E-scans) that permit rapid coverage with a tight focal spot. If the array is flat and linear, then the scan pattern is a simple B-scan. A sectorial-scan (S-scan) refers to either the beam movement or the data display. As a data display, the S-scan is a 2D view of all A-scans from a specific set of elements corrected for delay and refracted angle. When used to refer to the beam movement, it refers to

the set of focal laws that sweep through a defined range of angles using the same set of elements. One application for S-scans involves a stationary array, sweeping across a relatively inaccessible component like a welded area, to map out the features and defects. Dynamic Depth-Focusing is also a beamforming technique that allows changing the spatial response of the array, by moving the focal spot of the probe [33-35].

Sizing a defect detected through a simple B-scan and an S-scan is straightforward. However, if a curved array is used to perform an electronic scan of a corner (see Figure 1), then defect sizing in the index axis is not directly obtained from the B-scan, but must be calculated. The real size (*s*) of a defect in the index axis is a function of the apparent size *(C)*, as shown in the B-scan, the radius *(r)* and the thickness *(t)* of the corner, the radius of the probe *(R)* and the depth *(d)* of the defect below the surface. The reason for this is that the rectified cross-sectional view of the corner, represented in the resulting B-scan, inevitably distorts the appearance of any ultrasonic reflectors found within the material. Equations 1 and 2 show, respectively, the formulas for the inner diameter (ID) and outer diameter (OD) inspection approaches [36].

$$s = \frac{C \cdot (r+d)}{R} \qquad \text{Equ 1}$$

$$s = \frac{C \cdot (r+t-d)}{R} \qquad \text{Equ 2}$$

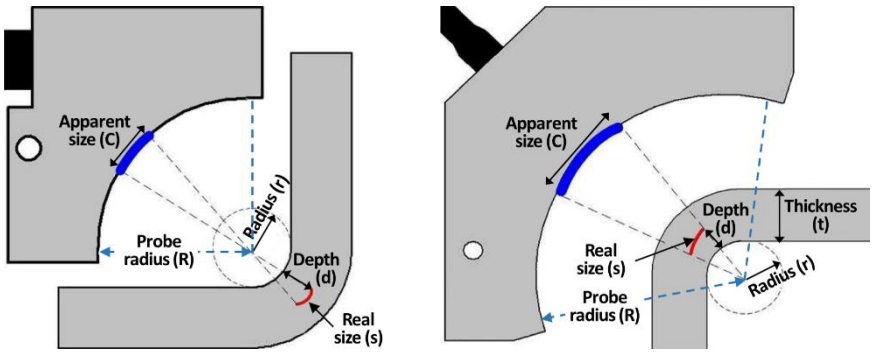

Figure 1 – Curved array performing an electronic scan of a corner, with ID (a) and OD (b) inspection approaches [36].

Equations 1 and 2 are simple algebraic formulas, which an NDT inspector can easily apply every time accurate sizing is required for each indication detected through radius phased array probes. The simplicity of such formulas to correct the geometrical distortion is due to the specific scenario, where the cylindrical probe aperture is positioned coaxially to the surface of the corner. In this case, all ultrasonic beam axes are perpendicular to the surface of the probe and hit the specimen surface perpendicularly too. However, simple correction formulas are not available for complex situations. The remaining part of this paper introduces a generalized algorithm to remove the geometrical distortions present in B-scans, which are constituted by a sequence of A-scans relative to ultrasonic beams that penetrate the part with variable incident angles.

3. B-scan correction algorithm

When a longitudinal ultrasonic wave strikes an interface between two different media, specific phenomena are observed. The wave is both reflected and refracted. If the second media is solid, a phenomenon known as mode conversion causes also the refracted ultrasonic energy to decompose into two waves: a shear wave (S) and a longitudinal wave (L) component. This work ignores the refracted shear wave, since it has low energy content for the range of considered

incident angles. Therefore, the original incident longitudinal beam is reflected and refracted by the interface between the two media, as it is well explained by the Fermat's principle developed in optics [37] and by the well-known Snell's law in acoustics [38].

The Snell's law describes, for isotropic materials, the relationship between the angles and the velocities of the waves. Snell's law equates the ratio of material velocities (V_{1L}, V_{2L} and V_{2S}) to the ratio of the sine of the angles (θ_{1L}, θ_{2L} and θ_{2S}) the wave propagation directions form with the normal to the interface at the incidence point, as shown in the following equation.

$$\frac{\sin\theta_{1L}}{V_{1L}} = \frac{\sin\theta_{2L}}{V_{2L}} = \frac{\sin\theta_{2S}}{V_{2S}} \quad \text{Equ 3}$$

Let us assign unitary intensity to the wave striking the interface between medium 1 and medium 2 with incidence angle θ_{1L}, thus producing refraction angles of longitudinal and shear waves respectively equal to θ_{2L} and θ_{2S}. The intensity of the reflected and refracted (transmitted) longitudinal waves, respectively indicated with I_{12}^{R} and I_{12}^{T}, can be computed using the following equations:

$$I_{12}^{R} = \left(\frac{Z_L cos^2 2\theta_{2S} + Z_S sin^2 2\theta_{2S} - Z_1}{Z_L cos^2 2\theta_{2S} + Z_S sin^2 2\theta_{2S} + Z_1}\right)^2 \quad \text{Equ 4}$$

$$I_{12}^{T} = \frac{\rho_1}{\rho_2}\frac{tan\theta_{1L}}{tan\theta_{2L}}\left(\frac{2\,Z_L \cos 2\theta_{2S}}{Z_L cos^2 2\theta_{2S} + Z_S sin^2 2\theta_{2S} + Z_1}\right)^2 \quad \text{Equ 5}$$

where $Z_1 = \rho_1 V_{1L}/cos\theta_{1L}$, $Z_L = \rho_2 V_{2L}/cos\theta_{2L}$ and $Z_S = \rho_2 V_{2S}/cos\theta_{2S}$, with ρ_1 and ρ_2 indicating the material densities [39].

Reflection, refraction, mode conversion and energy attenuation take place at each interface encountered between different media. When inspecting an isotropic and homogeneous part in ultrasonic pulse-echo mode, using the immersion technique, the ultrasonic beam encounters three interfaces during its path. After being generated by the transducer, the beam travels through water until striking the interface between the water and the front part surface (front wall), where part of the beam energy is refracted within the part material. The refracted beam continues its path within the volume of the part until it hits the interface at the other side of the part (back wall), where part of the refracted beam energy is reflected creating what is called "echo". Then the echo travels back to the front wall interface and the wave component, which is refracted at this interface, arrives back to the transducer surface and is finally converted into a measurable signal. Therefore, the refraction and reflection angles and the energy attenuation at every interface must be considered, through Equations 3-5, to verify the inspectability of a part with a given cross-sectional geometry.

Figure 2 shows the interactions between the ultrasonic longitudinal wave generated by a single element transducer (or by a single aperture in a phased array probe) and the interfaces of a solid part immersed in water. In Figure 2a and Figure 2b, the incident longitudinal wave (L_1) strikes the first interface between the water and the solid perpendicularly; part of its energy goes to the reflected wave (L_1^R) and the residual part to the transmitted wave (L_1^T). Part of the energy of L_1^T gets reflected at the back wall and forms the echo wave (L_E). In Figure 2a, L_E returns to the first interface and strikes it perpendicularly, producing the transmitted echo wave (L_E^T) that reaches the transducer. Conversely, the complex back-wall geometry in Figure 2b does not allow the back wall echo to return to the transducer, since L_E strikes the interface at an angle and the resulting wave refracted into water misses the receiving probe surface. In Figure 2c, for any point along the back wall and keeping constant the length (W) of the segment the incident wave travels in water, the probe is tilted by an angle. Such angle, calculated through Snell's law, produces a refracted longitudinal wave that arrives perpendicularly to the back wall. Then, L_1^T is optimally reflected by the back wall interface to form L_E, which follows the same path of

the incident wave in reverse. In this case, the amplitude (A) of L_E^T is always lower than the amplitude of the wave received in Figure 2a, because of the mode conversion at the first interface that disperses part of the energy into the shear wave (S_1^T). However, the approach in Figure 2c allows maximizing the amplitude of the echo receivable from any point along the complex back wall, when using the immersion pulse-echo inspection technique.

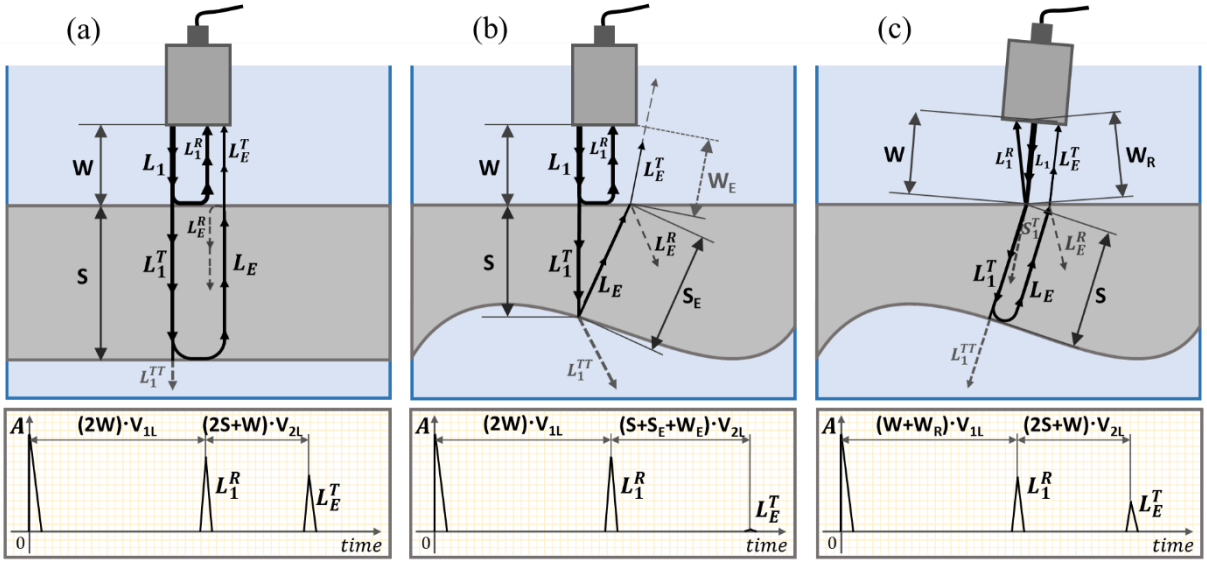

Figure 2 – Ultrasonic pulse-echo for simple (a) and complex back wall (b and c).

This work considers the approach represented in Figure 2c to map the back wall geometry. CIVA Software [40] has been used to simulate the beam propagation in an Aluminium sample. The water immersion pulse-echo technique was simulated, setting V_{1L} = 1483 m/s for the acoustic wave propagation velocity in water. The water path was set equal to W = 10 mm, in order to keep the probe near field (~7.6 mm) above the part front surface. Velocities equal to V_{2L} = 6360 m/s and V_{2S} = 3100 m/s were respectively set for the longitudinal and shear wave propagation speeds in aluminium. A cylindrical 3 mm diameter single element probe, with a flat active surface and a central frequency of 5MHz, was chosen for the CIVA simulations. The simulated A-scans were imported and processed in MATLAB®. The ultrasonic beams produced by a single element probe (in pulse-echo configuration) were simulated. The probe positions and orientations were calculated opportunely, in accordance with the Snell's law, in order to make sure the refracted wave (L_1^T), relative to each beam, strikes the back wall perpendicularly. Figure 3 shows a diagram reporting the problem tackled by this work. The area enclosed within the dotted rectangle is described in the remaining part of this paper.

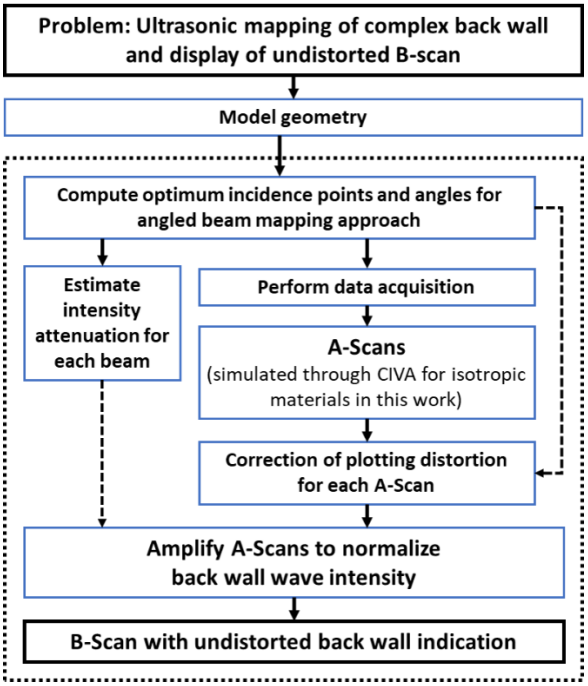

Figure 3 – Problem tackled by this work.

3.1 Geometric correction

The sample geometry, given in Figure 4, was imported in CIVA. It has a flat front surface and a curved back wall consisting of a quarter of 20 mm radius circumference, whose centre is located at 30 mm depth with respect to the front surface. Mapping 58 degrees arc of the back wall was simulated using parallel ultrasonic inspection beams (Figure 4a) and angled inspection beams (Figure 4c). For the parallel mapping approach, the transducer was moved at a constant step of 1 mm along the front surface. For the angled beam mapping approach, the transducer was translated and rotated by quantities suitable to produce longitudinal waves that strike the back wall perpendicularly at points separated by 1 mm long arc segments. Figure 4a and Figure 4c illustrate, for the sake of clarity, half of the resulting ultrasonic beams. The black arrows show the propagation paths. Whereas the back wall echoes do not return to the transducer for most of the back wall points for the case in Figure 4a, since the back wall reflects the beams in accordance with the Snell's law, the return paths always coincide with the forward paths in Figure 4c, where incident angles are calculated considering Equ 1. The vertical dashed lines illustrate the directions along which the resulting A-scans are displayed to form the traditional B-scan perpendicular to the scanning surface and parallel to a reference direction, as defined in the BS EN 1330-4:2000. This displays the B-scan (the model cross-section) on the plane through which the individual A-scans have been simulated, which contains the ultrasonic beam axes. Therefore, the resulting B-scans are overlaid to the part geometry in Figure 4b and Figure 4d. The B-scan are plotted with 50% transparency, to help assess the alignment between the B-scans and part geometry. The algorithm described in [28] has been used to triangulate the succession of A-scans points and visualize the B-scans as triangular meshes whose colour of the points corresponds to the A-scan original amplitude.

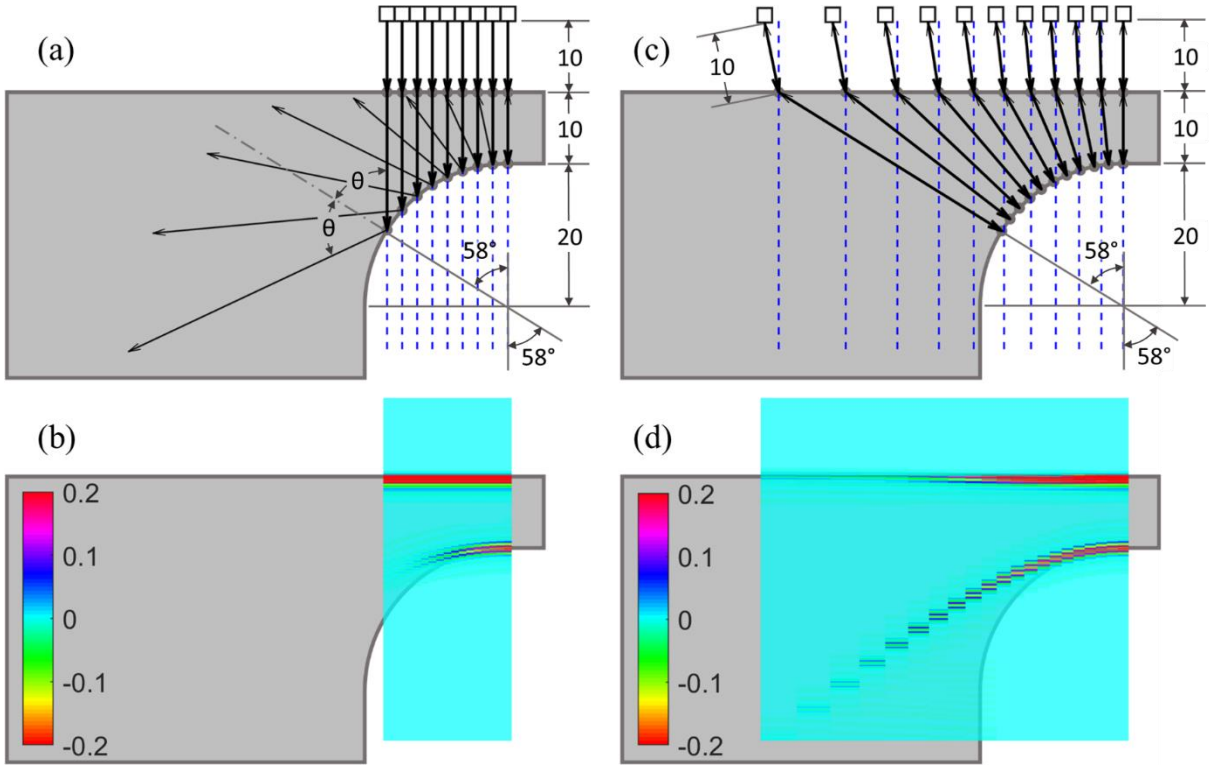

Figure 4 – Ultrasonic pulse-echo with parallel beams (a) and angled beams (c) and respective B-scans (b and d).

The angled beams produce stronger back wall echoes, as explained above. However, the relative B-Scan in Figure 4d is visibly distorted, since the back wall indications diverge from the reference geometry, due to the deviation between the real beam direction and the direction perpendicular to the front surface at the point of incidence. For this reason, an algorithm has been developed to resolve this geometrical distortion and improve the B-scan visualization. For clarity in the description of such algorithm, Figure 5 shows the original i-th A-scan and the same A-scan after the correction of the distortion. Let us indicate the point of incidence between the i-th beam and the front surface with $F_i \equiv [x_{F_i}, y_{F_i}]$ and consider the encoding positions of all A-Scan samples stored in the Nx2 matrix, $\boldsymbol{C^i} = [\boldsymbol{x^i} \quad \boldsymbol{y^i}]$, where N is the number of samples. The first column ($\boldsymbol{x^i}$) is an Nx1 vector of zeros. Since each original A-scan is displayed along the vertical direction, all points of the same A-scan share the same x-coordinate value, equal to x_{F_i}. The second column ($\boldsymbol{y^i}$) is the vector of the y-coordinates. This vector is the result of the manipulation of the sampling time vector ($\boldsymbol{t}$), as follows:

$$\boldsymbol{y^i} = -\begin{bmatrix} \left[\boldsymbol{t}(1{:}\,i_0) \cdot \frac{V_1}{2}\right] - W \\ \left[\boldsymbol{t}(i_0+1{:}\,N) \cdot \frac{V_2}{2}\right] - W \end{bmatrix} \qquad \text{Equ. 6}$$

where i_0 is the index of the last sample collected above the front surface.

Indicating with $\boldsymbol{R_1^i}$ and $\boldsymbol{R_2^i}$ the matrices of rotation around the z-axis (perpendicular to the B-scan plane), respectively corresponding to the angles θ_{1L}^i and θ_{2L}^i, the corrected matrix of encoding coordinates, $\boldsymbol{C_C^i}$, is given by:

$$\boldsymbol{C_C^i} = \begin{bmatrix} \left[\boldsymbol{x^i}(1{:}\,i_0) - x_{F_i} \quad \boldsymbol{y^i}(1{:}\,i_0)\right] * \boldsymbol{R_1^i} \\ \left[\boldsymbol{x^i}(i_0+1{:}\,N) - x_{F_i} \quad \boldsymbol{y^i}(i_0+1{:}\,N)\right] * \boldsymbol{R_2^i} \end{bmatrix} + [\boldsymbol{x_{F_i}} \quad \boldsymbol{o}] \qquad \text{Equ. 7}$$

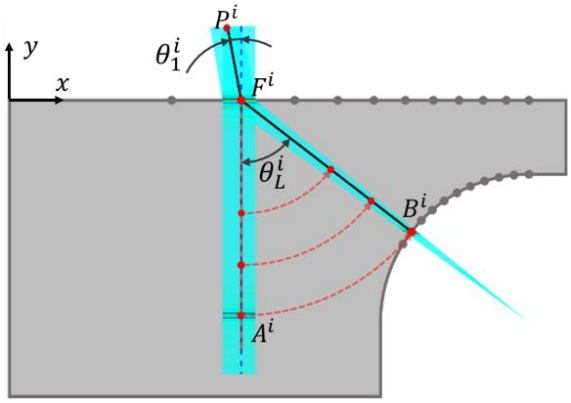

Figure 5 – Correction of the i-th A-scan display.

Using the corrected encoding positions to plot the i-th A-scan provides alignment to the originating ultrasonic beam path. Applying Equ. 6 and 7 to all A-scans that form the B-scan, an undistorted version of the B-scan is obtained (Figure 6a). This corrected result clearly shows the elimination of the geometric distortion.

3.2 Intensity correction

The amplitude (or intensity) of the back wall reflection is visibly changing along the 58 degree arc. The amplitude decreases from right to left, both for the case of parallel beams and angled beams. Assuming unitary energy for all incidence beams, the variable amplitude is caused by the different attenuation experienced by the beams during their travel. For the case of parallel beams ($\theta_{1L} = \theta_{2L} = \theta_{2S} = 0$), from Equ. 4 and 5 it is possible to find that all transmitted beams (L_1^T), produced at the interface between medium 1 (water) and medium 2 (Aluminium), have the same intensity, since they strike the interface of two isotropic media with the same incidence angle. The decreasing amplitude visible in Figure 6a is caused by the variable incidence angle between L_1^T and the back wall, between L_E and the interface between solid and water and by the fact the return point of L_E^T to the transducer surface diverges from the surface centre. This latter element alone causes a strong decay of the return wave amplitude and any a posteriori amplification is impractical, since it would produce a poor signal-to-noise ratio.

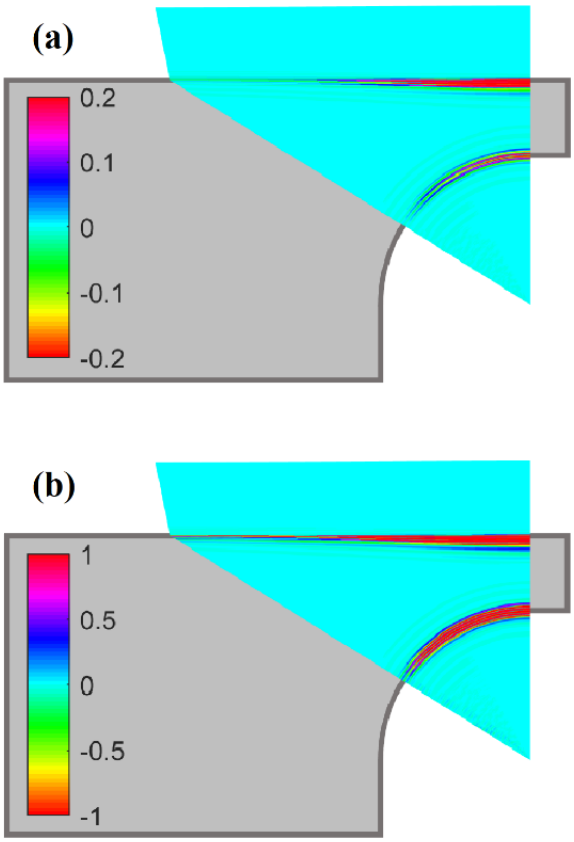

Figure 6 – Correction of geometric distortion (a) and of back wall amplitude (b).

Conversely, for the case of angled beam, where each incident beam has a different incidence angle and produces different longitudinal and shear refraction angles, the reflected and transmitted beams will inherit different (but predictable) energy portions. In relation to the unitary amplitude of the i-th incident beam, the intensity of L_E^{Ti} that comes back to the transducer is estimated by the following formula:

$$I^i = I_{12}^{Ti} \cdot I_{21}^{Ri} \cdot I_{21}^{Ti} \qquad \text{Equ 11}$$

where I_{12}^{Ti} is the intensity attenuation factor of the wave transmitted from water to solid, I_{21}^{Ri} is the attenuation factor of the wave reflected at the back wall (the interface between material 2 and material 1), and I_{21}^{Ti} is the attenuation experienced by the returning echo at the front interface between solid and water. Figure 7 shows the plot of attenuation (in decibels [dB]) relative to such factors and the total attenuation, I^i. The attenuations are given versus the incidence angle (spanning between zero and the first critical angle, as shown at the top horizontal axis) and the refracted angle (shown at the bottom horizontal axis). The opposite of the total attenuation is used as gain to correct the intensity of the A-scans that form the B-scan.

Therefore, the final corrected B-scan is given in Figure 6b. The amplification of the A-scans that form the B-scan has the effect of normalizing the intensity of the back wall echoes. Thus, it is important to notice the colour bar limits have been extended from -1 to 1, in Figure 6b. For refracted angles smaller than 60 degrees in immersion pulse-echo of aluminium samples, which is the case considered in this work, the required amplification is always smaller than 40 dB.

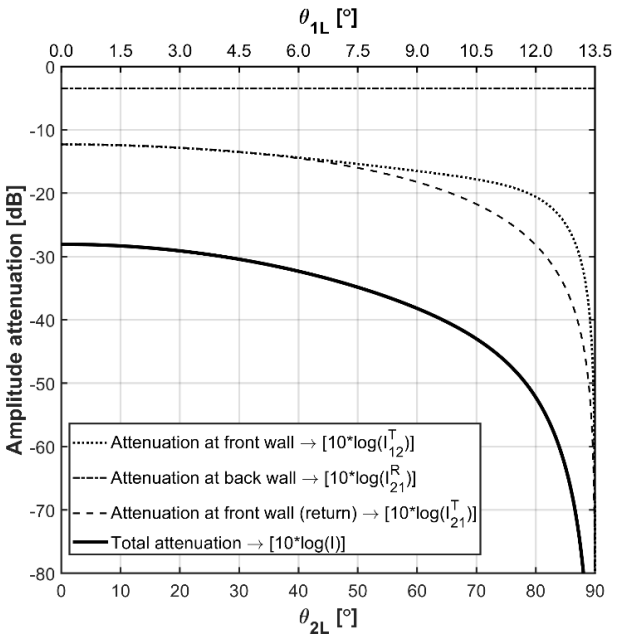

Figure 7 – Plot of the attenuation factors (in decibels [dB]). The opposite value of the total attenuation is used as gain to correct the intensity of the B-scan.

3.3 Application to a more complex back wall

The application of the developed algorithm to a more complex back wall is now presented. The new geometry is shown in Figure 8.

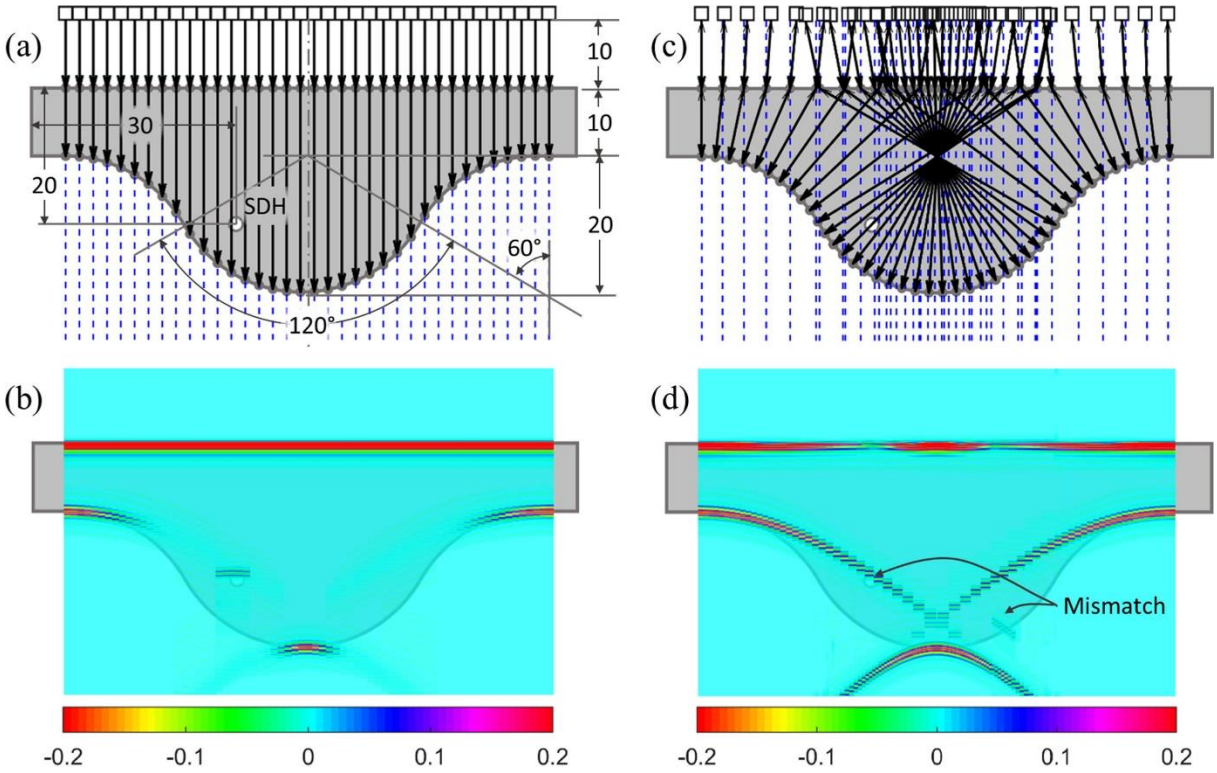

Figure 8 – Mapping of a complex back wall, through simulated ultrasonic pulse-echo with parallel beams (a) and angled beams (c) and respective B-scans (b and d).

The sample model has a flat front surface and a curved back wall consisting in two 60 degree arcs of 20 mm radius circumference, separated by a 120 degree arc with the same radius circumference but opposite curvature. This geometry more closely resembles the back wall

profile of a stiffening stringer in aerospace structures. A 2 mm diameter side-drilled hole (SDH) has been included, located at 30mm from the left hand side corner of the model and at a depth of 20mm. The same Aluminium material has been considered, having the acoustic properties defined above. The same probe was considered, simulating the ultrasonic wave propagation through CIVA. Mapping of the back wall was simulated using the standard parallel ultrasonic inspection beams (Figure 8a) and the angled inspection beams (Figure 8c). For the parallel mapping approach, the transducer was moved at a constant step of 1 mm along the front surface. Although this approach gives a clear echo from the SDH, the back wall is almost not mapped. For the angled beam mapping approach, explained above, the transducer was translated and rotated by quantities suitable to produce longitudinal waves that are incident on the back wall perpendicularly at points separated by 1 mm long arc segments. The incident angles were opportunely calculated, according to the Snell's law, through Equ 1. In Figure 8d, the mismatch between the B-Scan data and the geometry of the sample is evident. The reflection wave from the simulated SDH is dislocated from the position of the modelled defect. Applying the introduced approach for correction of geometry and amplitude distortion, the resulting B-scans in Figure 9a and Figure 9b are obtained. The two anomalies in the back wall echo are caused by the interference of the front surface secondary echo, which distorts the reflection from the back wall. The echo from the 2mm diameter SDH is correctly scaled and positioned.

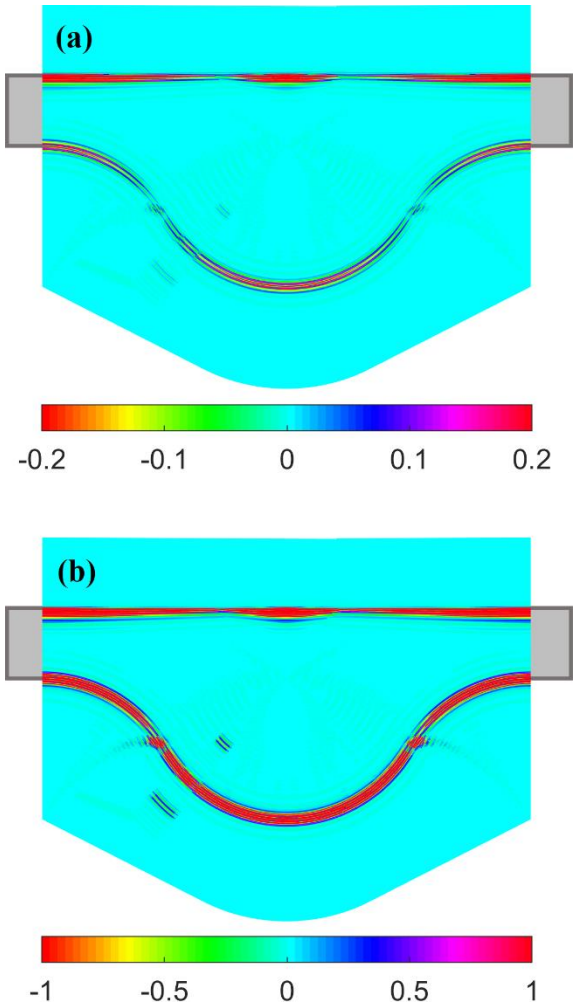

Figure 9 – Correction of geometric distortion (a) and of back wall amplitude (b) for a model with complex back wall and SDH.

4. Conclusion and future work

Ultrasonic imaging of complex back wall is currently challenging. This work has introduced a novel approach to improve the ultrasonic inspectability of parts with complex back walls. Conventional approaches for ultrasonic inspection for such parts require separate inspections of both surfaces. Using ultrasonic phased array probes and state-of-the-art instrumentation allows for sending ultrasonic energy into a part at wide ranges of focusing depths and steering angles. This allows tracking the back wall profile, thus hitting it at normal incidence and hence maximizing the amplitude of the reflected echo at any point. This work has shown that a cross-sectional scan resulting from multiple ultrasonic beams, which are sent at variable incidence angles, present significant geometrical distortion and are of limited use for accurate defect visualization and sizing. This paper introduced a generalized algorithm able to remove geometric distortions and the effect that variable attenuation factors have on the received amplitudes. Future work will extend the approach (currently for isotropic materials) to consider anisotropic composite materials. The ultimate goal is to enable the possibility to map complex back walls from the front wall side (a typical application being the inspection of in-service components, where only a single side access is usually possible). The correction algorithm will also be extended to B-scan correction for focused ultrasonic beams produced by concave surface single element probes and by phased array probes.

Acknowledgements

This work was funded by Spirit AeroSystems Ltd (Prestwick, Scotland, UK). We also acknowledge additional support received from the Autonomous Inspection in Manufacturing and Re-Manufacturing (AIMaReM) project, funded by the UK Engineering and Physical Science Research Council (EPSRC) through the grant EP/N018427/1.

References

[1] T. Kundu, *Ultrasonic Nondestructive Evaluation*: CRC Press, 2003.

[2] R. Huang, "Ultrasonic modeling for complex geometries and materials," Engineering Mechanics, Iowa State University, Ames, Iowa, 2006.

[3] G. A. Deschamps, "Ray techniques in electromagnetics," *Proceedings of the IEEE,* vol. 60, pp. 1022-1035, 1972.

[4] C. Holmes, B. W. Drinkwater, and P. D. Wilcox, "Post-processing of the full matrix of ultrasonic transmit–receive array data for non-destructive evaluation," *NDT & E International,* vol. 38, pp. 701-711, 2005.

[5] M. Sutcliffe, M. Weston, P. Charlton, K. Donne, B. Wright, and I. Cooper, "Full matrix capture with time-efficient auto-focusing of unknown geometry through dual-layered media," *Insight-Non-Destructive Testing and Condition Monitoring,* vol. 55, pp. 297-301, 2013.

[6] M. Parrilla, A. Ibáñez, J. Camacho, and C. Fritsch, "Fast focal law computing for Non-Destructive Testing with phased arrays," in *International Congress on Ultrasonics*, 2007, pp. 1-4.

[7] A. J. Hunter, B. W. Drinkwater, and P. D. Wilcox, "Autofocusing ultrasonic imagery for non-destructive testing and evaluation of specimens with complicated geometries," *NDT & E International,* vol. 43, pp. 78-85, 2010.

[8] S. Chatillon, S. Mahaut, and P. Dubois, "Simulation of Advanced UT Phased Array Techniques with Matrix Probes and Dynamic Settings for Complex Component Inspections," 2009.

[9] E. Hoyle, M. Sutcliffe, P. Charlton, and J. Rees, "Virtual source aperture imaging with auto-focusing of unknown complex geometry through dual layered media."

[10] C. N. MacLeod, S. G. Pierce, M. Morozov, R. Summan, G. Dobie, P. McCubbin, *et al.*, "Automated metrology and NDE measurements for increased throughput in aerospace component manufacture," in *41st annual review of progress in Quantitative Nondestructive Evaluation*, 2015, pp. 1958-1966.

[11] T. Sattar, "Robotic non-destructive testing," *Industrial Robot: An International Journal,* vol. 37, 2010.

[12] D. L. Hopkins, M. Brassard, G. A. Neau, J.-N. Noiret, W. V. Johnson, and L. L. Ber, "Surface-Adaptive Ultrasound (SAUL) for phased-array inspection of composite specimens with curved edges and complex geometry."
[13] S. Robert, O. Casula, O. Roy, and G. Neau, "Real-Time Inspection of Complex Composite Structures with a Self-Adaptive Ultrasonic Technique."
[14] F. Bentouhami, B. Campagne, E. Cuevas, T. Drake, M. Dubois, T. Fraslin, *et al.*, "LUCIE - A flexible and powerful Laser Ultrasonic system for inspection of large CFRP components.," presented at the 2nd International Symposium on Laser Ultrasonics, Talence (France), 2010.
[15] A. Maurer, W. D. Odorico, R. Huber, and T. Laffont, "Aerospace composite testing solutions using industrial robots," presented at the 18th World Conference on Nondestructive Testing, Durban, South Africa, 2012.
[16] J. T. Stetson and W. D. Odorico, "Robotic inspection of fiber reinforced aerospace composites using phased array UT," presented at the 40th Annual Review of Progress in Quantitative NDE, Baltimore, Maryland, 2013.
[17] C. Mineo, S. Pierce, B. Wright, I. Cooper, and P. Nicholson, "PAUT inspection of complex-shaped composite materials through six DOFs robotic manipulators," *Insight-Non-Destructive Testing and Condition Monitoring*, vol. 57, pp. 161-166, 2015.
[18] E. Cuevas, S. Hernandez, and E. Cabellos, "Robot-Based Solutions for NDT Inspections: Integration of Laser Ultrasonics and Air Coupled Ultrasounds for Aeronautical Components," in *25th ASNT Research Symposium*, 2016, pp. 39-46.
[19] R. A. Smith, "Use of 3D ultrasound data sets to map the localised properties of fibre-reinforced composites," 2010.
[20] C. Mineo, S. G. Pierce, P. I. Nicholson, and I. Cooper, "Robotic path planning for non-destructive testing–A custom MATLAB toolbox approach," *Robotics and Computer-Integrated Manufacturing*, vol. 37, pp. 1-12, 2016.
[21] M. Brassard, D. L. Hopkins, and J. N. Noiret, "Integration of Robotics and Surface Adaptive Phased Array UT to Achieve Fully Automated Inspection of Complex Composite Parts."
[22] C. Mineo, C. MacLeod, M. Morozov, S. G. Pierce, T. Lardner, R. Summan, *et al.*, "Fast ultrasonic phased array inspection of complex geometries delivered through robotic manipulators and high speed data acquisition instrumentation," in *Ultrasonics Symposium (IUS), 2016 IEEE International*, 2016, pp. 1-4.
[23] C. Mineo, C. MacLeod, R. Su, D. Lines, S. Davì, B. Cowan, *et al.*, "Robotic Geometric and Volumetric Inspection of High Value and Large Scale Aircraft Wings," presented at the 2019 IEEE International Workshop on Metrology for AeroSpace, Turin (Italy), 2019.
[24] R. Su, C. Mineo, C. N. MacLeod, S. G. Pierce, and A. Gachagan, "Multi-aperture beamforming for automated large structure inspection using ultrasonic phased arrays," in *AIP Conference Proceedings*, 2019, p. 100009.
[25] J. Zhang, B. W. Drinkwater, and P. D. Wilcox, "Efficient Immersion Imaging of Components With Nonplanar Surfaces."
[26] D. Hopkins, M. Datuin, and M. Brassard, "Challenges and solutions for ultrasonic phased-array inspection of polymer-matrix composites at production rates."
[27] A. Maurer, W. Deodorico, R. Huber, and T. Laffont, "Aerospace Composite Testing Solutions using Industrial Robots," 2012.
[28] C. Mineo, J. Riise, R. Summan, C. N. MacLeod, and S. G. Pierce, "Index-based triangulation method for efficient generation of large three-dimensional ultrasonic C-scans," *Insight-Non-Destructive Testing and Condition Monitoring*, vol. 60, pp. 183-189, 2018.
[29] J. Camacho, J. F. Cruza, J. Brizuela, and C. Fritsch, "Automatic Dynamic Depth Focusing for NDT," *IEEE Transactions on Ultrasonics, Ferroelectrics, and Frequency Control*, vol. 61, pp. 673 - 684, April 2014.
[30] J. F.Cruza, J. Camacho, J. M.Moreno, and C. Fritsch, "Ultrafast hardware-based focal law calculator for automatic focusing," *NDT&E International*, 2015.
[31] O. Casula, C. Poidevin, G. Cattiaux, and P. Dumas, "Control of Complex Components with Smart Flexible Phased Arrays," pp. 829 - 836.
[32] J. M. Davis and M. Moles, "Resolving capabilities of phased array sectorial scans (S-scans) on diffracted tip signals," *Insight-Non-Destructive Testing and Condition Monitoring*, vol. 48, pp. 233-239, 2006.
[33] J. Camacho, J. F. Cruza, J. Brizuela, and C. Fritsch, "Automatic Dynamic Depth Focusing for NDT," *IEEE Transactions on Ultrasonics, Ferroelectrics, and Frequency Control*, vol. 61, April 2014.

[34] D. CASSEREAU, "Focusing with ultrasonic phased arrays - comparison between timedelay laws and time-reversal," in *Proceedings 2000 IEEE International Conference on Phased Array Systems and Technology (Cat. No.00TH8510)*.
[35] J. F. Cruza, J. Camacho, L. Serrano-Iribarnegaray, and C. Fritsch, "New Method for Real-Time Dynamic Focusing Through Interfaces," *IEEE Transactions on Ultrasonics, Ferroelectrics, and Frequency Control*, vol. 60, pp. 739 - 751.
[36] O. Report, "PA probe and radius wedges for composite inspection."
[37] Olympus. *Introduction to phased array ultrasonic technology applications*. Available: https://www.olympus-ims.com/en/books/pa/pa-intro/
[38] B. A. Auld, *Acoustic fields and waves in solids* vol. 2: John Wiley & Sons, 1973.
[39] J. D. N. Cheeke. (2012). *Fundamentals and Applications of Ultrasonic Waves (2nd ed.)*.
[40] P. Calmon, S. Mahaut, S. Chatillon, and R. Raillon, "CIVA: An expertise platform for simulation and processing NDT data," *Ultrasonics*, vol. 44, pp. e975-e979, 2006.